

Single-atom maser with engineered circuit for population inversion

A.A. Sokolova,^{1,2,3,*} G.P. Fedorov,^{1,2,3} E.V. Il'ichev,^{4,1} and O.V. Astafiev^{5,2,6,7}

¹*Russian Quantum Center, Skolkovo village, Russia*

²*Moscow Institute of Physics and Technology, Dolgoprudny, Russia*

³*National University of Science and Technology MISIS, Moscow, Russia*

⁴*Leibniz Institute of Photonic Technology, 07745 Jena, Germany*

⁵*Skolkovo Institute of Science and Technology, Moscow, Russia*

⁶*Physics Department, Royal Holloway, University of London, Egham, Surrey TW20 0EX, United Kingdom*

⁷*National Physical Laboratory, Teddington, TW11 0LW, United Kingdom*

(Dated: October 2020)

We present a blueprint for a maser with a single three-level transmon superconducting artificial atom. The system can be pumped coherently via a two-photon process, and to achieve high population inversion, the relaxation rate of the metastable state is increased via an auxiliary low-Q cavity coupled to a transition between the transmon excited states. We show numerically that such a maser can operate both in the intermediate coupling regime with super-Poissonian photon statistics and in the strong coupling regime, where the statistics is sub-Poissonian. For the former, the maser exhibits thresholdless behavior and for the latter, there is a well-defined pumping threshold. A useful side-effect of the auxiliary resonator is that it allows to overcome the photon blockade effect for the pump, which would otherwise prevent high photon population. Finally, we observe the bistability of the steady-state Wigner function and the self-quenching effect for some parameters.

I. INTRODUCTION

Conventional multi-atom lasers operate in the regime of weak coupling between the atoms and the light modes, possess a threshold and emit classical light. Single-atom lasers with strong coupling have been gaining increased attention since 1990s, as their behavior was predicted to be drastically different from usual lasers [1–12]. Among their non-standard features are presence or absence [9, 10] of the pumping threshold depending on the parameters [13]; self-quenching, when the cavity population decreases when the pumping rate is increased [1]; photon blockade prohibiting coherent pumping of more than a single photon in the strong-coupling regime [13–17]; bistability of the Wigner function [18, 19]; sub-Poissonian statistics of the emitted radiation leading to amplitude squeezing and purely quantum phenomena such as photon antibunching or super-Poissonian statistics with high intensity fluctuations and phase squeezing [1]. Owing to these peculiar properties, a single-atom laser may be used for a wide range of applications as a source of non-classical radiation [20–25].

Experimentally, the first single-atom maser has been implemented in 1985 on Rydberg atoms [26]. Then, several other platforms for single-atom lasing have been proposed, including trapped ions [13, 27], trapped Cs atom [28, 29], quantum dots [30–32], superconducting single-electron transistors [18, 33] and flux qubits [34–36]. The single-atom masers based on superconducting cQED devices are particularly interesting since they can be used in tandem with superconducting artificial atoms [37].

In this work, we present a blueprint for a maser in this architecture using a transmon-type artificial atom [38]. The transmon may be regarded as a Ξ -system with the eigenstates

$|g\rangle, |e\rangle, |f\rangle$ referred to the ground, first and second excited states, respectively. The lasing transition $|e\rangle \rightarrow |g\rangle$ is in resonance with the reservoir lasing cavity coupled to the transmon. A classical lasing scheme in quantum optics is based on a Lambda-configuration of a three-level atom [1]. However, transmon is a cascade system and cannot be excited directly to the second excited state, and thus the pumping is done via two-photon excitation of the $|g\rangle \leftrightarrow |f\rangle$ transition. The pumping processes for population inversion may be described as $|g\rangle \xrightarrow{2\hbar\omega} |f\rangle \rightarrow |e\rangle$. However, due to the small non-linearity of the transmon the $|f\rangle \rightarrow |e\rangle$ process is only $\sqrt{2}$ times faster than $|e\rangle \rightarrow |g\rangle$. Therefore, to increase the effective pumping rate, we suggest to couple the transmon to another low-Q cavity resonant with the $|f\rangle \rightarrow |e\rangle$ transition, very similar to what was done before for a chain of transmons [39]. This cavity plays a role of artificial bath [40–43], which relaxes the system to $|e\rangle$, ensuring the metastability of $|f\rangle$. Then, we solve the master equation numerically for the full system and study its transient and steady-state behavior for various combinations of parameters.

The suggested model is different from those studied before at least in two ways. First, we use a two-photon process for coherent pumping. Second, we employ engineered $|f\rangle \rightarrow |e\rangle$ dissipation via an auxiliary resonator, which at the same time significantly modifies the system spectrum. Actually, the latter fact alleviates the effect of the photon blockade [14] caused by the large size of the vacuum Rabi splittings in the strong coupling regime [3], similar to the case of the cascade laser proposed in 1995 [44]. This effect allows to pump more than 40 photons in the strong-coupling regime. A similar breakdown of the photon blockade was investigated before in a simpler Jaynes-Cummings system [45].

Additionally, our simulations predict that depending on its parameters, the system can be operated in two distinct regimes. In one regime we observe a well-defined lasing threshold in our architecture which we also associate with the unusual energy level structure and blockade breakdown. In

* Sokolova.aa@phystech.edu

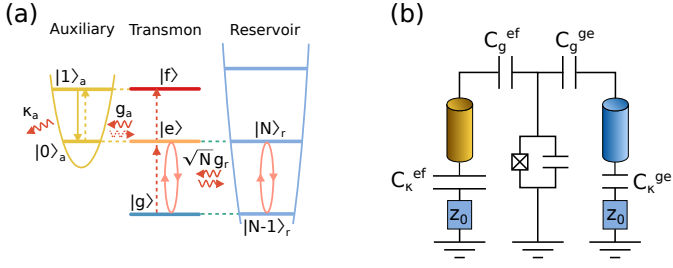


FIG. 1. **(a)** Schematic configuration of the correctly aligned energy levels without coupling between subsystems. The reservoir is resonant with the $|g\rangle \leftrightarrow |e\rangle$ transition, and the auxiliary cavity is resonant with the $|e\rangle \leftrightarrow |f\rangle$ transition. $|g\rangle, |e\rangle, |f\rangle$ are in blue (medium gray), orange (light gray) and red (dark gray), respectively. **(b)** Schematic of the circuit. To the left is the auxiliary and to the right is the reservoir cavity. C_g^{ge} (C_g^{ef}) is a capacitor that couples transmon with reservoir (auxiliary) cavity, and C_{κ}^{ge} (C_{κ}^{ef}) – capacitor that provides the desired external quality factor

the other, no threshold is present, and there is a phase transition between the regimes with a sharp increase of the steady-state cavity population and the intensity fluctuations. A similar transition between different lasing regimes was previously predicted for the strong coupling [18, 46].

II. MODELING THE SYSTEM

The scheme of the system is shown conceptually in Fig. 1 (a). A tunable transmon is coupled to two cavities: the reservoir (right) and the auxiliary (left) with the coupling strengths g_r and g_a , respectively. The reservoir has high internal and external Q-factors and should accumulate a considerable number of photons being in resonance with the $|g\rangle \leftrightarrow |e\rangle$ transition of the transmon, at frequency ω_{ge} . The second low-Q cavity is resonant with the $|e\rangle \leftrightarrow |f\rangle$ transition at frequency ω_{ef} , and thus provides an engineered metastability of the $|f\rangle$ -state. The cavities do not interact directly with each other. To describe this system we apply the Jaynes-Cummings model [47] with an obvious modification to include two cavities, and in the rotating wave approximation (RWA) the resulting Hamiltonian reads:

$$\hat{H} = \hat{H}_t + \hat{H}_d + \sum_{\lambda=r,a} (\hat{H}_c^{(\lambda)} + \hat{H}_i^{(\lambda)}), \quad (1)$$

$$\hat{H}_t = \hbar\Delta b^\dagger b + \frac{\hbar\alpha}{2} b^\dagger b (b^\dagger b - 1), \quad (2)$$

$$\hat{H}_d = \frac{\hbar\Omega}{2} (b + b^\dagger), \quad (3)$$

$$\hat{H}_c^{(\lambda)} = \hbar\Delta_c^{(\lambda)} (a_\lambda^\dagger a_\lambda + 1/2), \quad (4)$$

$$\hat{H}_i^{(\lambda)} = \hbar g_\lambda (b a_\lambda^\dagger + b^\dagger a_\lambda), \quad (5)$$

where \hat{H}_t , \hat{H}_d , $\hat{H}_c^{(\lambda)}$ and $\hat{H}_i^{(\lambda)}$ are transmon, drive, cavity and interaction Hamiltonians, respectively, and a_r , a_a , b are the standard bosonic annihilation operators for the reservoir,

auxiliary resonator and the transmon, respectively. The transmon parameters are: $\Delta = \omega_{ge} - \omega_d$, the detuning of drive frequency ω_d from the $|g\rangle \leftrightarrow |e\rangle$ transition; $\alpha < 0$, the anharmonicity; Ω , the microwave drive amplitude. Next, $\Delta_c^{(r,a)} = \omega_{r,a} - \omega_d$ are the detunings of the reservoir and auxiliary cavities, respectively. In the ideal configuration, when the reservoir is resonant with the $|g\rangle \leftrightarrow |e\rangle$ transition, the auxiliary cavity is resonant with the $|e\rangle \leftrightarrow |f\rangle$ transition, and the drive is at the two-photon frequency $\omega_d = \omega_{gf}/2 = \omega_{ge} + \alpha/2$, we can find $\Delta_c^r = \Delta = -\alpha/2$ and $\Delta_c^a = \alpha/2$.

Since relaxation processes are essential for lasing, modeling the system requires solution of the full Lindbladian master equation: for the transmon, the reservoir, and the auxiliary cavity, we use the relaxing collapse operators $\sqrt{\gamma}\hat{b}$, $\sqrt{\kappa_r}\hat{a}_r$, $\sqrt{\kappa_a}\hat{a}_a$, respectively.

To demonstrate the feasibility of the proposed device, we evaluate also its physical parameters. The optimal values for $g_{r,a}$, $\kappa_{r,a}$, ω_d were found with a Nelder-Mead algorithm aimed at maximizing the emitted power from the reservoir calculated by the input-output theory [48]:

$$P = \kappa_r N_{ss} \cdot \hbar\omega_{ge}, \quad (6)$$

where N_{ss} is the steady-state number of photons in the reservoir. In our simulations, truncating the reservoir Fock space at 60 photons, we find the optimal parameters to be the following: $g_r/2\pi = 6.5$ MHz, $g_a/2\pi = 23.5$ MHz, $\kappa_r = 0.31 \mu\text{s}^{-1}$, $\kappa_a = 138 \mu\text{s}^{-1}$ and $\omega_d = \omega_{gf}/2$, for $\Omega/2\pi = 25$ MHz. The algorithm converges to the same values starting from different initial parameters, so there is probably a single optimum in the parameter space. Since κ_a is much larger than the two-photon Rabi frequency (see below for details), the number of photons in auxiliary cavity stays close to zero on average, so we truncate its Fock space to one photon. For the optimization, we use fixed realistic values for $\gamma = 0.1 \mu\text{s}^{-1}$, $\omega_{ge}/2\pi = 6$ GHz, $\alpha/2\pi = -200$ MHz, $\omega_r/2\pi = 6$ GHz, and $\omega_a/2\pi = 5.8$ GHz. For the optimal parameters we found $N_{ss} = 49$, which corresponds to -132 dBm of emitted power.

Fabricating the superconducting cavities and the transmon with megahertz accuracy in frequency and anharmonicity should be experimentally attainable, and then the ideal configuration can be reached by tuning the transmon into the resonance with the reservoir via the external magnetic flux. Schematically, the circuit model of the device is shown in Fig. 1 (b).

The reservoir population is tolerant to small changes of the parameters, which can occur during fabrication. N_{ss} becomes lower, but still enough to measure, due to mismatch between the auxiliary resonator frequency and $|e\rangle \leftrightarrow |f\rangle$ transition up to 30 MHz, while $|g\rangle \leftrightarrow |e\rangle$ frequency of the transmon can be always tuned directly to resonance with the reservoir cavity. The changes of κ_a do not affect N_{ss} significantly: higher κ_a does not change N_{ss} at all, while up to 40% lower κ_a still allows for pumping enough photons to measure. Variation of g_r and g_a affects the population significantly but slowly (see below for details), so their deviation from ideal values also should not be a problem. The only parameter whose deviation significantly affects the maser is κ_r : the lower κ_r allows for

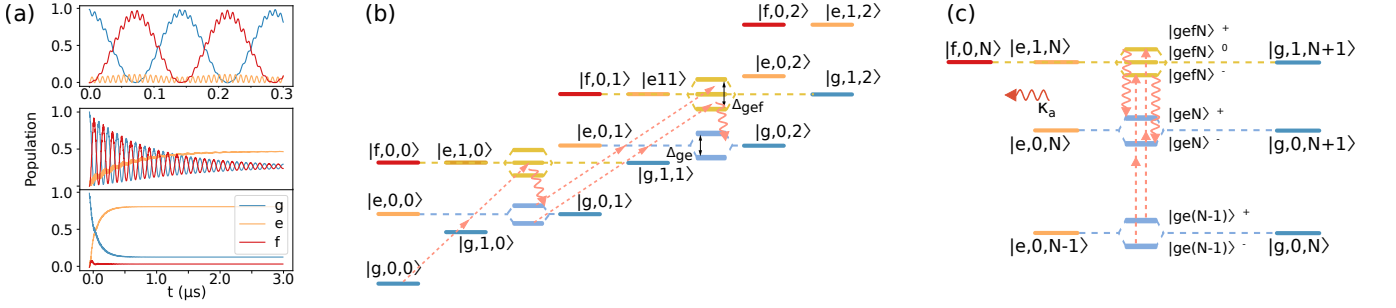


FIG. 2. (a) Population of the transmon levels under a two-photon drive, $\Omega/2\pi = 25$ MHz. Upper panel: $\gamma = 0$, $g_a = 0$, middle panel: $\gamma = 1 \mu\text{s}^{-1}$, $g_a = 0$, lower panel: $\gamma = 1 \mu\text{s}^{-1}$, $g_a/2\pi = 8$ MHz, $\kappa_a = 138 \mu\text{s}^{-1}$. (b) Low-energy subspace of the system spectrum. Dashed arrows show two-photon pumping, wavy arrows – relaxation processes. Blue (medium gray) levels correspond to $|g\rangle$, orange (light gray) – $|e\rangle$, red (dark gray) – $|f\rangle$. (c) A single pumping stage showing transition from $N - 1$ to N photons in the reservoir and the participating eigenstates.

pumping much more photons, but higher κ_r may completely prohibit lasing. However, higher κ_r can be coped with by increasing g_r .

In addition, we have verified that adding dephasing to the transmon with γ_ϕ in the range of one μs^{-1} and even tens of μs^{-1} does not alter the number of pumped photons significantly.

III. PUMPING DYNAMICS

To calculate numerically the dynamics of the system, we use the QuTiP Python package [49]. Below we denote the factorized states of the tripartite system as $|\mu, M, N\rangle$ where μ is the transmon state (g, e, f), and M, N are the number of photons in the auxiliary resonator and the reservoir, respectively. To facilitate the interpretation of the simulation results, we split the task into several steps.

First of all, we simulate the transmon under a two-photon drive by turning off the coupling to the cavities and the dissipation. The simulated evolution is shown in the upper panel of Fig. 2 (a) (here and below we truncate the transmon subspace to four states). One can clearly see two-photon Rabi oscillations when the $|f\rangle$ energy level is fully populated by the two-photon process. There are also small oscillations of the $|e\rangle$ -level population from the virtual processes.

In the middle panel Fig. 2 (a), we add natural relaxation to the transmon. The rate of the $|f\rangle \rightarrow |e\rangle$ transition is higher n_{12}/n_{01} times than of the $|e\rangle \rightarrow |g\rangle$ one, where n_{ij} is matrix element of charge operator in the basis of transmon eigenstates [38]. In this case, some population inversion may be achieved without any additional effort. Nevertheless, when the coupling to the auxiliary cavity it turned on, the population inversion becomes significantly larger, as shown in the lower panel of Fig. 2 (a).

Finally, we turn on the coupling to the reservoir cavity. The resulting level structure of the full tripartite system is depicted in Fig. 2(b), and Fig. 2(c) shows the core process of pumping an additional photon in the reservoir. One can see that there are two types of Rabi splittings in the spectrum. The first, caused by the interaction between the reservoir and the $|g\rangle \leftrightarrow$

$|e\rangle$ transition of the transmon, leads to the formation of the

$$|geN\rangle^\pm = \frac{1}{\sqrt{2}}(|g, 0, N + 1\rangle \pm |e, 0, N\rangle) \quad (7)$$

dressed states composed of the factorized states with different reservoir populations. To avoid ambiguity, we label them using the lower number N . The size of this splitting is calculated as

$$\Delta_{ge}(N) = 2g_r\sqrt{N + 1}. \quad (8)$$

The second splitting is due to the coupling between three degenerate states $|f, 0, N\rangle$, $|e, 1, N\rangle$, and $|g, 1, N + 1\rangle$. When the degeneracy is lifted, triplet eigenstates appear:

$$|gefN\rangle^0 = \sin\theta |g, 1, N + 1\rangle - \cos\theta |e, 1, N\rangle, \quad (9)$$

$$|gefN\rangle^\pm = \frac{1}{\sqrt{2}}(\cos\theta |g, 1, N + 1\rangle \pm |e, 1, N\rangle + \sin\theta |f, 0, N\rangle), \quad (10)$$

where

$$\tan\theta = \frac{g_a}{g_r\sqrt{N + 1}} \quad (11)$$

is the mixing angle. The energy difference between $|gefN\rangle^+$ and $|gefN\rangle^-$ is

$$\Delta_{gef}(N) = 2\sqrt{(N + 1)g_r^2 + g_a^2}. \quad (12)$$

As before, we label the triplet states by the lowest N among their factorized components.

We note that the first splitting (Eq. 8) is ordinary for any coupled atom-cavity system and grows as \sqrt{N} with photon population of the cavity [50]. In contrast, the second one (Eq. 12) is the characteristic feature of our system due to the presence of the auxiliary resonator and a certain frequency configuration. As we show below, both these splittings play the crucial role in the dynamics and allow the device to function in principle for arbitrarily large reservoir populations.

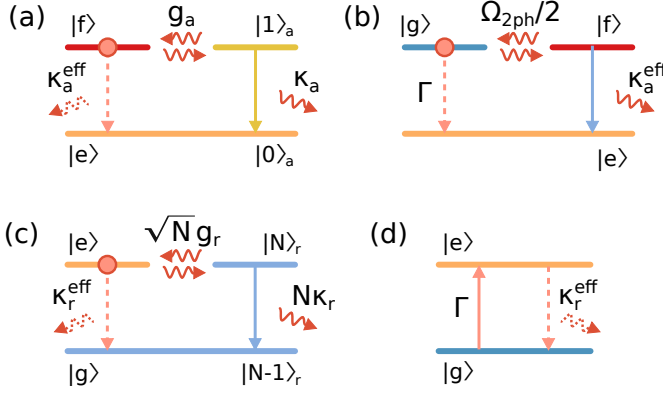


FIG. 3. (a) Estimating the effective relaxation rate κ_a^{eff} due to the auxiliary cavity. (b) Estimating the effective pumping rate due to the two-photon drive Ω_{2ph} and the effective relaxation κ_a^{eff} . (c) Estimating the effective relaxation rate due to the reservoir with N photons inside. (d) $|g\rangle$ and $|e\rangle$ levels of transmon with effective $|e\rangle \rightarrow |g\rangle$ dissipation, which act as a two-level laser.

IV. SIMPLIFIED ANALYTICAL SOLUTION

To calculate approximately the reservoir population in the steady state, we consider only the $|g\rangle$ and $|e\rangle$ states with the effective pumping rate Γ and effective dissipation rate κ_r^{eff} through the reservoir (Fig. 3(d)). In this simplified view, the balance condition $\kappa_r^{\text{eff}} = \Gamma$ allows to determine the reservoir population when the pumping ceases since κ_r^{eff} is proportional to N and Γ is constant. We prove this in several steps below.

Firstly, we calculate the effective $|f\rangle \rightarrow |e\rangle$ relaxation rate due to the auxiliary cavity (Fig. 3(a)). Consider two coupled two-level systems: the first two-level system (on the left) represents $|e\rangle$ and $|f\rangle$ levels of transmon, and the second one (on the right) – $|0\rangle$ and $|1\rangle$ levels of the auxiliary resonator. The relevant master equation for a Hamiltonian $H = g_a(ba_a^\dagger + a_a b^\dagger)$ with a collapse operator $\sqrt{\kappa_a}a_a$ assuming initial state $|f\rangle$ has separate analytical solutions for the underdamped and overdamped regimes.

In the underdamped, or strong coupling regime when $4g_a > \kappa_a$, the population of $|f\rangle$ is

$$\rho_{ff} = \frac{e^{-\frac{\kappa_a t}{2}}}{\cos^2 \theta} \cos^2(g't + \theta), \quad (13)$$

where $g' = \sqrt{16g_a^2 - \kappa_a^2}/4$, $\tan \theta = \frac{\kappa_a}{g'}$. Using the decay rate of the vacuum Rabi oscillations, one may assume that

$$\kappa_a^{\text{eff}} = \frac{\kappa_a}{2}. \quad (14)$$

In the overdamped, or weak coupling regime where $4g_a < \kappa_a$,

$$\rho_{ff} = \frac{e^{-\frac{\kappa_a t}{2}}}{\cosh^2 \theta} \cosh^2(\gamma't + \theta), \quad (15)$$

where $\gamma' = \sqrt{\kappa_a^2 - 16g_a^2}/4$, $\tan \theta = \frac{\kappa_a}{\gamma'}$. The decay rate is

determined by the slowest exponent, so

$$\kappa_a^{\text{eff}} = \frac{\kappa_a - \sqrt{\kappa_a^2 - 16g_a^2}}{2}. \quad (16)$$

One can see that while g_a is fixed, increasing κ_a at first increases but then decreases κ_a^{eff} upon transition from the underdamped to the overdamped regime ($\kappa_a^{\text{eff}} \rightarrow 4g_a^2/\kappa_a$ there). Physically, this effect can be explained by the broadening of the $|1\rangle_a$ level, which prevents transfer of energy from $|f\rangle$. Thus, κ_a^{eff} reaches its maximum when $\kappa_a = g_a$ which is consistent with our numerical simulations.

Next, we calculate effective $|g\rangle \rightarrow |e\rangle$ pumping rate Γ . The simplified model of the system with two-photon pumping and $|f\rangle \rightarrow |e\rangle$ dissipation is shown on Fig. 3(b). The two-photon process is replaced by the equivalent one-photon drive of strength Ω_{2ph} (see Appendix A for details). This step is only approximate as it does not take into account the full complexity of the energy spectrum and the possibility of the off-resonant two-photon drive. From Fig. 3(b) one can see that the tree-level system with pumping and dissipation is completely equivalent to the two coupled two-level systems in Fig. 3(a) with g_a replaced by $\Omega_{2ph}/2$. The solution for the such a system is the same: in the strong coupling regime $2\Omega_{2ph} > \kappa_a^{\text{eff}}$ the effective pumping rate is

$$\Gamma = \frac{\kappa_a^{\text{eff}}}{2}, \quad (17)$$

and for the weak coupling regime $2\Omega_{2ph} < \kappa_a^{\text{eff}}$

$$\Gamma = \frac{\kappa_a^{\text{eff}} - \sqrt{(\kappa_a^{\text{eff}})^2 - 4\Omega_{2ph}^2}}{2}. \quad (18)$$

In our case, the strong coupling is not achievable due to the weakness of the two-photon drive. Consequently, we take Eq. 18 to calculate effective pumping rate. For the optimal parameters from section II, it leads to $\Gamma = 5.3$ MHz.

The next step is the calculation of effective dissipation rate κ_r^{eff} due to the reservoir populated with N photons (Fig. 3(c)). Again, the system is equivalent to Fig. 3(a). Coupling strength g_r should not be much lower than g_a , otherwise the Rabi splittings will disturb pumping (see next section for detail). Assuming this, for optimal g_a and $\kappa_r < 1 \mu\text{s}^{-1}$, the condition for the strong coupling regime $4\sqrt{N}g_r > N\kappa_r$ is met even for high reservoir populations ($N \sim 100$). Therefore,

$$\kappa_r^{\text{eff}} = \frac{N_{ss}\kappa_r}{2}. \quad (19)$$

The energy balance condition is $\kappa_r^{\text{eff}} = \Gamma$ (Fig. 3(d)). Consequently, the maximum number of pumped photons can be expressed as

$$N_{ss} = 2 \frac{\Gamma}{\kappa_r}. \quad (20)$$

For the optimal parameters, this equation gives $N_{ss} = 34$. The exact simulated value is $N_{ss} = 49$. The 30% difference is probably caused by the differences in the real level structure due to the coupling to both cavities.

V. OVERCOMING PHOTON BLOCKADE

The simplified model studied in the previous section does not take into account the effects of the photon blockade as it replaces the coherent pumping by an effective incoherent one. However, the auxiliary cavity actually allows to treat the system within the simplified model. To see this, one should first consider a simple device that does not include an auxiliary resonator, operates in the strong-coupling regime and is subject to photon blockade as follows. Due to the \sqrt{N} growth of the $\Delta_{ge}(N)$, there is no single frequency that would satisfy the resonance condition of the two-photon pumping for an arbitrary population of the reservoir. The pumping at the $|g, 0, N\rangle \leftrightarrow |f, 0, N\rangle$ frequency becomes off-resonant when $\langle \hat{N} \rangle = \langle a_r^\dagger a_r \rangle \geq 1$ [3] (see Fig. 2 (b)) as there would be no triplet Rabi splittings and the detuning would be $\delta = \Delta_{ge}(N)/2$. This effect is observed for all coherently pumped single-atom lasers: $\delta = g_r \sqrt{N} \rightarrow \infty$ for $N \rightarrow \infty$ [14].

However, in the presence of the auxiliary resonator one can see from Fig. 2 (b,c) that the detuning of the two-photon drive is instead calculated as

$$\delta = [\Delta_{gef}(N+1) - \Delta_{ge}(N)]/2 \quad (21)$$

One can see that $\delta \rightarrow 0$ for $N \rightarrow \infty$ (Fig. 2(c)), which means that it would be possible to use monochromatic pumping at $\omega_{gf}/2$ for sufficiently large values of $\langle \hat{N} \rangle$, even though it would be slightly off-resonant for low $\langle \hat{N} \rangle$. In other words, if it is possible to pump several photons in the reservoir off-resonantly, then the subsequent pumping will become resonant and similar to the simplified model. We demonstrate numerically that the latter is possible due to the large dissipative bandwidths of the states in the $|gefN\rangle^{\pm,0}$ splittings. The low Q-factor of the auxiliary resonator allows off-resonant transitions to them even if the detuning is of the order of several MHz. In Fig. 4 (a, b), we compare the steady-state solution with the transient solutions at 1 and 2 μs . The steady-state picture shows that pumping at a frequency close to $|g, 0, 0\rangle \leftrightarrow |f, 0, 0\rangle$ is indeed optimal in the long term, despite that at first the sideband $|geN\rangle^+ \leftrightarrow |gefN\rangle^+$ has a higher pumping rate, see Appendix A for details; the sidebands are subject to the photon blockade and eventually die off for large $\langle \hat{N} \rangle$.

As a result, with optimal parameters, we can pump ≈ 50 photons while maximizing output power (-132 dBm at the optimum). Maximizing the reservoir population allows pumping at least 90 photons in the steady state (above this point, the simulation becomes intractable due to the size of the necessary Hilbert space).

VI. DIFFERENT LASING REGIMES AND PHASE TRANSITIONS

While the simplified model is applicable for large reservoir populations, numerical solution is required to accurately

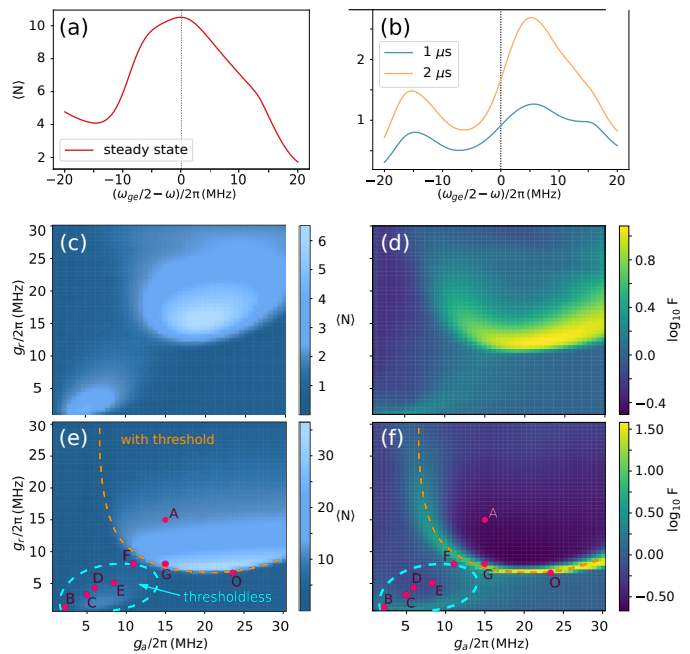


FIG. 4. (a, b) Average number of photons in the reservoir depending on the drive frequency ω for $g_r/2\pi = g_a/2\pi = 15$ MHz, $\kappa_r = 0.2 \mu s^{-1}$, $\kappa_a = 128 \mu s^{-1}$, $\Omega/2\pi = 20$ MHz (point A in (e, f)) in the steady state (a) and in 1 μs and 2 μs after the pumping was started (b). (c, e) Pumped photons and (d, f) logarithm of Fano factor vs. coupling strengths for $\kappa_a = 138 \mu s^{-1}$, $\kappa_r = 0.2 \mu s^{-1}$. (c, d) $\Omega/2\pi = 15$ MHz, (e, f) $\Omega/2\pi = 20$ MHz. The letters are different sets of the parameters used in the other subsections (O depicts the optimal parameters). Orange dashed line marks the transition to the threshold-bearing regime and blue dashed line the thresholdless regime.

characterize the behavior of the system for arbitrary parameter combinations. We find that the most important parameters are the coupling strengths between the transmon and the cavities, so in this section we study in detail how they affect the reservoir steady state properties.

Fig. 4(c-f) shows the reservoir population and the logarithm of the Fano factor $F = \frac{\langle N^2 \rangle - \langle N \rangle^2}{\langle N \rangle}$ in the steady state depending on $g_{r,a}$ for two different values of Ω . F is a measure of intensity fluctuations of the laser field: $F < 1$ indicates sub-Poissonian statistics and photon antibunching, $F = 1$ – coherent Poissonian field, and $F > 1$ – super-Poissonian statistics with high intensity fluctuations.

For both driving strengths, one can see an area with a significant increase in the N_{ss} and F when the coupling strengths $g_{r,a}$ become large enough. We find that this area marks the phase transition between two regimes of lasing: threshold-bearing and threshold-less (see section VII for detail). The lasing threshold is said to exist if there is some pumping power value for which a rapid increase of intensity fluctuations and usually of the steady-state photon number in the cavity is observed [10].

For the smaller drive amplitude, the phase transition is not very pronounced; however, for the larger drive, it is sharp (or-

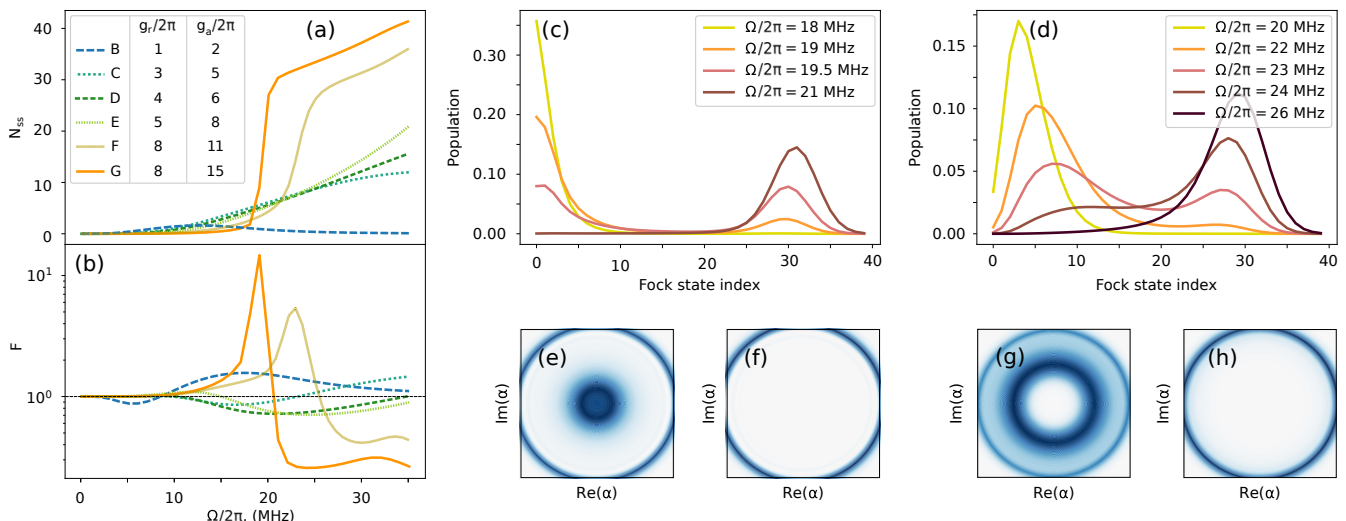


FIG. 5. Reservoir population **(a)** and the Fano-factor **(b)** for the threshold-less and threshold-bearing regimes (points B-F in Fig. 4, values for $g_{a,r}/2\pi$ in the legend are in MHz). For all panels $\kappa_a = 138 \mu\text{s}^{-1}$, $\kappa_r = 0.2 \mu\text{s}^{-1}$. **(c-d)** Reservoir Fock state probability for various Ω : **(c)** point G, **(d)** point F. **(e-h)** Steady-state reservoir Wigner functions: **(e)** for (c), $\Omega/2\pi = 19.5$ MHz; **(f)** for (c), $\Omega/2\pi = 21$ MHz; **(g)** for (d), $\Omega/2\pi = 23$ MHz; **(h)** for (d), $\Omega/2\pi = 26$ MHz.

ange dashed line). After the transition, the lasing is characterized by the large N_{ss} and $F < 1$. Finally, the area of the threshold-bearing regime grows when the pumping rate is increased.

Qualitatively, the location of the threshold-bearing regime in the parameter space can be explained as follows. Firstly, the large coupling constant g_r allows pumping the reservoir quicker, which explains why the transition requires $g_r/2\pi$ to exceed 12 and 8 MHz, for the weak and strong drive, respectively. Secondly, when $g_a/2\pi < 8$ MHz, the coupling to the auxiliary resonator is too low to reach significant κ_a^{eff} and to produce sufficient population inversion. Finally, increasing g_a while keeping g_r fixed reduces N_{ss} due to the increasing detuning discussed in section V.

In the thresholdless regime in the bottom left corner of Fig. 4(c, e) (dashed blue line) it is still possible to pump a considerable number of photons (about 5-10) while $F \gtrsim 1$ in this area. This regime is standard for single-atom lasers in the intermediate and low-coupling regime. The coupling constants in the thresholdless regime are low, so the energy splittings $\Delta_{ge}(N)$ and $\Delta_{gef}(N)$ do not play any role due to the dissipative line broadening.

VII. THRESHOLD AND BISTABILITY

Single-atom lasers previously discussed in literature were thresholdless in the strong coupling regime [10, 13, 28], but could have one or two thresholds in the regime of weak and intermediate coupling [13, 27, 51]. Therefore, below we discuss why in our case it is possible to observe a threshold even in the strong coupling regime.

Fig. 5(a, b) shows the steady-state values for N_{ss} and F for five different combinations of coupling constants, corre-

sponding to points B-F in Fig. 4 (e, f), depending on the drive amplitude Ω . For the first four sets of parameters (B-E), there is no well-defined threshold, even for $g_r/2\pi = 5$ MHz, $g_a/2\pi = 8$ MHz (E), which has a small maximum of F at $\Omega/2\pi = 12$ MHz. The photon distribution in the regimes B-E can be super-Poissonian as well as sub-Poissonian depending on the drive power. The observed behavior is consistent with previous works [9, 51].

For the combination B, $g_r/2\pi = 1$ MHz and $g_a/2\pi = 2$ MHz, we observe self-quenching probably caused by the dressing of the energy levels by the strong drive. This effect is still not clear to us, because self-quenching remains even if we manually tune pumping frequency into resonance with the correct transition to one of the dressed states, even though the maximum of pumped photons shifts to the larger Ω .

The most interesting feature in Fig. 5 (a),(b) is the presence of a well-defined threshold for the combination G: $g_r/2\pi = 8$ MHz and $g_a/2\pi = 15$ MHz and F: $g_r/2\pi = 8$ MHz and $g_a/2\pi = 11$ MHz. Our simulations show that such a threshold is present for any point above the orange dashed line at Fig. 4 (e, f). Above the threshold, for some parameters there is also no manifestations of the photon blockade – the average number of photons increases steadily with growing Ω . As mentioned above, this is different from the previous results for single-cavity systems with coherent pumping in the strong-coupling regime [27, 29].

Fig. 5 (c, e, f) illustrate the cavity state in the vicinity of the threshold for the point G, and Fig. 5 (d,g,h) – for the point F. One can see bistability which manifests itself as a double-peak structure of the Wigner function. At a sufficiently high driving power for the bistability to vanish, only the outer ring of Wigner function remains and the Fano factor is significantly lower than one.

We explain the bistability in the studied system as follows.

We consider the intermediate cavity states with N approximately between 2 and 25 for Fig. 5 (c) and between 5 and 25 for Fig. 5 (d). These states can not be populated via the coherent pump due to the large detuning they have due to vacuum Rabi splittings (see Eq. 21), and the relaxation dominates their population dynamics. However, the upper states can be pumped resonantly, as discussed before, so the system can remain there indefinitely. Therefore, with increasing drive strength the higher levels gradually absorb more and more of the population from the lower ones as the population is leaking better and better through the “blocked” states. In the middle of the threshold transition, this results in the apparent bimodal distribution of photons and very high intensity fluctuations. Additionally, in Appendix B, we show that bistability would not be observed if the Rabi-splittings did not depend on the photon number.

This mechanism resembles the one studied in [52], where the high-order multiphoton processes are becoming closer and closer to each other in frequency, while the single-photon processes are prone to photon blockade. Additionally, the similar mechanism was experimentally confirmed in [45], where the photon blockade in the strong-coupled qubit-resonator system was broken by the weakly-coupled third level of the qubit, making resonant pumping of the cavity possible.

VIII. CONCLUSION

In this work, we studied theoretically a single-atom maser based on two-photon coherent pumping of a transmon. We find that to attain high population inversion, one needs to artificially increase the relaxation rate of its $|e\rangle \rightarrow |f\rangle$ transition and show that this is feasible by coupling it to an auxiliary low-Q resonator.

Our master equation simulations predict two distinct regimes of operation for the device with the presence or absence of the lasing threshold. The boundary between the regimes is determined by the coupling strengths between the transmon and the cavities.

In the threshold-less regime, our system demonstrates non-classical behavior similar to the previously known for single-atom lasers, including both sub-Poissonian and super-Poissonian statistic, and self-quenching.

In the other regime, for which the coupling strengths are higher, we observe a well-defined lasing threshold, marked by an increase of intensity fluctuations. We associate its presence with the interplay between the photon blockade and the peculiarities of the energy spectrum caused by the auxiliary resonator, and the consequent bistability of Wigner function. The light statistics in the reservoir in this regime is highly sub-Poissonian, with $F < 0.5$, and its population is of order of tens of photons.

Finally, via numerical optimization, we find an optimal set of parameters for a device that allows pumping about 50 photons in the strong-coupling regime, which corresponds to -132 dBm of emitted power. The statistics in this regime is predicted to be sub-Poissonian with $F = 0.27$. We believe that due to the non-classical properties such maser may have

a wide range of applications for microwave quantum optics on a chip [20, 21, 23].

IX. ACKNOWLEDGMENTS

The investigation was conducted with the support of Russian Science Foundation, Grant No. 16-12-00095. We also acknowledge support from the Ministry of Education and Science of the Russian Federation in the framework of the Increased Competitiveness Program of the National University of Science and Technology MISIS (Contract No. K2-2020-022).

Appendix A: Estimated pumping rate of the two-photon process

The frequency of the two-photon Rabi oscillations for a three-level system is generally calculated as [53]

$$\Omega_{2ph} = \frac{\Omega^2}{2\Delta}, \quad (\text{A1})$$

where Δ is the detuning between the pump frequency and the intermediate level. In our case, this is the detuning between ω_d and the splitted energy levels $|geN\rangle^\pm$ (Fig. 2(d)). In case of $|g, 0, 0\rangle \leftrightarrow |f, 0, 0\rangle$ pumping $\Delta = \alpha/2$. For $|ge0\rangle^\pm \leftrightarrow |gef1\rangle^\pm$ -pumping

$$\Delta^\pm = \frac{\alpha}{2} \mp \frac{\Delta_{gef}(1) + \Delta_{ge}(0)}{4},$$

which we will call the “plus” and “minus” transitions. This leads to the fact that for the parameters in Fig. 4(a, b) the two-photon pumping rate of $|gef0\rangle^+$ level is 1.9 times higher than of $|gef0\rangle^-$ level. Since the pumping rate for the “plus” transition is higher than for the “minus” one for any N , in Fig. 4(a, b) the line corresponding to the “plus” transition is much brighter compared to the “minus” at the beginning of pumping. When $N \rightarrow \infty$, the frequencies of both types of transitions becomes equal, since $\delta \rightarrow 0$ (Eq. 21). So, it is not possible to distinguish them in the steady state picture in Fig. 4(a, b).

Appendix B: Role of level splittings in bistability

In Fig. 6 (a), the population of the resonator-reservoir for various Ω is shown. One can see that the intermediate states 5-25 are never populated. We have checked that they are also never populated during the full time evolution while the second peak just grows steadily similarly to what is shown in Fig. 6 (a) for increasing Ω .

In the main text, we explain the bistability by the large detuning of the intermediate pumping transition. To check if the unusual steady state is really caused by the detuning of these intermediate transitions, we have constructed an artificial interaction Hamiltonian of the reservoir and the transmon. In

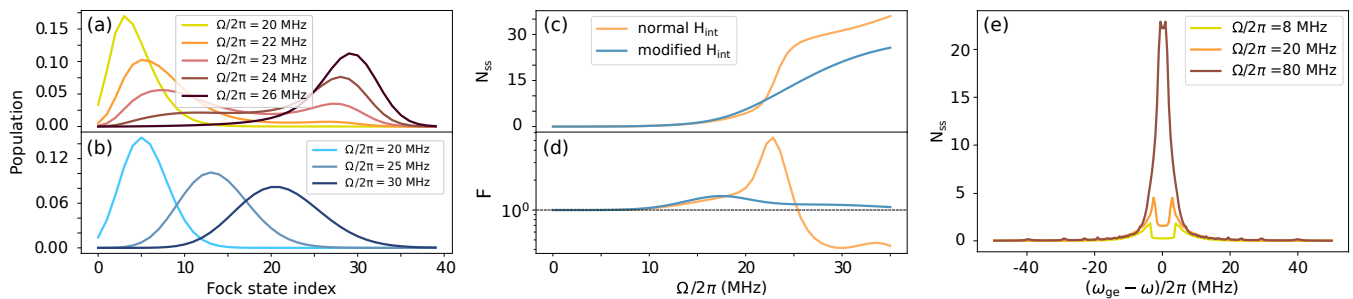


FIG. 6. Visualized reservoir states for the system with the following parameters: $\kappa_a = 138 \mu\text{s}^{-1}$, $\kappa_r = 0.2 \mu\text{s}^{-1}$, $g_r/2\pi = 8 \text{ MHz}$, $g_a = 11 \text{ MHz}$ (point F at Fig. 4(e, f), for different Ω . (a) With ordinary interaction Hamiltonian, (b) with modified interaction Hamiltonian. (c,d) Number of photons in the reservoir (c) and Fano factor (d) for ordinary and modified interaction Hamiltonian. (e) Number of photons in the reservoir depending on the detuning of the drive frequency ω from a frequency of reservoir resonator ω_{ge} . The system is modified such a way that allows only one-photon direct reservoir pumping: the number of the transmon states is truncated to 2, when $g_r/2\pi = 8 \text{ MHz}$, $g_a = 0$ and the other parameters are the same as in Fig. 5.

the new Hamiltonian, the annihilation operator is replaced by a lowering operator with unity matrix elements so the detuning does not depend on the number of photons in resonator any more. The steady states for such a system are shown in Fig. 6 (b). One can see that now there is only one peak and no bistability.

We have also simulated $\langle N \rangle$ and F in the steady state depending on Ω in Fig. 6 (c,d). One can see that a peak of F , which follows the threshold and present for the system with normal H_{int}^r ($F \approx 5$), is absent for the system with modified H_{int}^r . Consequently, the threshold, discussed in the main text, is indeed connected with special energy level structure and bistability.

Appendix C: Direct pumping of the cavities

One can expect that for large enough Ω the reservoir can be pumped by direct off-resonant drive, causing $|g, 0, N\rangle \rightarrow$

$|g, 0, N + 1\rangle$ transition. Thus, there could be a restriction on the value of Ω , after which the lasing breaks down. We now check if this supposition is correct.

We set g_a to zero and truncate the number of transmon states to 2. As a result, we have a two-level qubit coupled to the reservoir. Then we drive transmon at the frequency close to $|g\rangle \leftrightarrow |e\rangle$ transition, which is equal to the frequency of the reservoir, and observe the number of photons in the steady state of the reservoir depending on the detuning from this frequency, see Fig. 6(e). Even for a very strong drive of 80 MHz, the pumping becomes negligible when the detuning is just 20 MHz. In the suggested device, the detuning is $\omega_{ge} - \omega_d = 100 \text{ MHz}$, so the direct pumping of the reservoir should not be possible even for high Ω .

The direct pumping of the auxiliary cavity is not expected to be possible due to the same reasons, especially given that its relaxation rate is significantly higher than that of the reservoir. We have checked that the line broadening due to the large κ_a is not enough to make possible pumping with 100 MHz detuning.

-
- [1] Y. Mu and C. M. Savage, One-atom lasers, *Physical Review A* **46**, 5944 (1992).
 - [2] C. Ginzel, H.-J. Briegel, U. Martini, B.-G. Englert, and A. Schenzle, Quantum optical master equations: The one-atom laser, *Physical Review A* **48**, 732 (1993).
 - [3] T. Pellizzari and H. Ritsch, Preparation of stationary fock states in a one-atom raman laser, *Physical review letters* **72**, 3973 (1994).
 - [4] T. Pellizzari and H. Ritsch, Photon statistics of the three-level one-atom laser, *Journal of Modern Optics* **41**, 609 (1993).
 - [5] P. Horak, K. M. Gheri, and H. Ritsch, Quantum dynamics of a single-atom cascade laser, *Physical Review A* **51**, 3257 (1995).
 - [6] M. Löffler, G. M. Meyer, and H. Walther, Spectral properties of the one-atom laser, *Physical Review A* **55**, 3923 (1997).
 - [7] G. M. Meyer, M. Löffler, and H. Walther, Spectrum of the ion-trap laser, *Physical Review A* **56**, R1099 (1997).
 - [8] G. M. Meyer and H.-J. Briegel, Pump-operator treatment of the ion-trap laser, *Physical Review A* **58**, 3210 (1998).
 - [9] B. Jones, S. Ghose, J. P. Clemens, P. R. Rice, and L. M. Pedrotti, Photon statistics of a single atom laser, *Physical Review A* **60**, 3267 (1999).
 - [10] P. R. Rice and H. J. Carmichael, Photon statistics of a cavity-qed laser: A comment on the laser–phase-transition analogy, *Physical Review A* **50**, 4318 (1994).
 - [11] S. Y. Kilin and T. B. Karlovich, Single-atom laser: Coherent and nonclassical effects in the regime of a strong atom-field correlation, *Journal of Experimental and Theoretical Physics* **95**, 805 (2002).
 - [12] S. Ashhab, J. R. Johansson, A. M. Zagoskin, and F. Nori, Single-artificial-atom lasing using a voltage-biased superconducting charge qubit, *New Journal of Physics* **11**, 023030 (2009).
 - [13] F. Dubin, C. Russo, H. G. Barros, A. Stute, C. Becher, P. O. Schmidt, and R. Blatt, Quantum to classical transition in a

- single-ion laser, *Nature Physics* **6**, 350 (2010).
- [14] K. M. Birnbaum, A. Boca, R. Miller, A. D. Boozer, T. E. Northup, and H. J. Kimble, Photon blockade in an optical cavity with one trapped atom, *Nature* **436**, 87 (2005).
- [15] A. Imamoglu, H. Schmidt, G. Woods, and M. Deutsch, Strongly interacting photons in a nonlinear cavity, *Physical review letters* **79**, 1467 (1997).
- [16] E. Ginossar, L. S. Bishop, D. I. Schuster, and S. M. Girvin, Protocol for high-fidelity readout in the photon-blockade regime of circuit qed, *Physics Review A* **82**, 022335 (2010).
- [17] M. D. Reed, L. DiCarlo, B. R. Johnson, L. Sun, D. I. Schuster, L. Frunzio, and R. J. Schoelkopf, High-fidelity readout in circuit quantum electrodynamics using the jaynes-cummings nonlinearity, *Physics Review Letters* **105**, 173601 (2010).
- [18] D. A. Rodrigues, J. Imbers, and A. D. Armour, Quantum dynamics of a resonator driven by a superconducting single-electron transistor: A solid-state analogue of the micromaser, *Physical review letters* **98**, 067204 (2007).
- [19] M. Marthaler, J. Leppäkangas, and J. H. Cole, Lasing, trapping states, and multistability in a circuit quantum electrodynamical analog of a single-atom injection maser, *Physical Review B* **83**, 180505(R) (2011).
- [20] M. A. Nielsen and I. Chuang, *Quantum computation and quantum information* (2002).
- [21] D. L. Andrews, *Photonics, Volume 1: Fundamentals of Photonics and Physics* (John Wiley & Sons, 2015) pp. 121–164.
- [22] V. D’ambrosio, N. Spagnolo, L. D. Re, S. Slussarenko, Y. Li, L. C. Kwek, L. Marrucci, S. P. Walborn, L. Aolita, and F. Sciarrino, Photonic polarization gears for ultra-sensitive angular measurements, *Nature Communications* **4** (2013).
- [23] I. R. Berchera and I. P. Degiovanni, Quantum imaging with sub-poissonian light: challenges and perspectives in optical metrology, *Metrologia* **56**, 024001 (2019).
- [24] G. Brida, M. Genovese, and I. R. Berchera, Experimental realization of sub-shot-noise quantum imaging, *Nature Photonics* **4**, 227 (2010).
- [25] S. Pogorzalek, K. G. Fedorov, M. Xu, A. Parra-Rodriguez, M. Sanz, M. Fischer, E. Xie, K. Inomata, Y. Nakamura, E. Solano, A. Marx, F. Deppe, and R. Gross, Secure quantum remote state preparation of squeezed microwave states, *Nature Communications* **10** (2019).
- [26] D. Meschede, H. Walther, and G. Müller, One-atom maser, *Physical review letters* **54**, 551 (1985).
- [27] G. Meyer, H.-J. Briegel, and H. Walther, Ion-trap laser, *EPL (Europhysics Letters)* **37**, 317 (1997).
- [28] J. McKeever, A. Boca, A. D. Boozer, J. R. Buck, and H. J. Kimble, Experimental realization of a one-atom laser in the regime of strong coupling, *Nature* **425**, 268 (2003).
- [29] A. D. Boozer, A. Boca, J. R. Buck, J. McKeever, and H. J. Kimble, Comparison of theory and experiment for a one-atom laser in a regime of strong coupling, *Physical Review A* **70**, 023814 (2004).
- [30] N. Lambert, F. Nori, and C. Flindt, Bistable photon emission from a solid-state single-atom laser, *Physical review letters* **115**, 216803 (2015).
- [31] Y.-Y. Liu, J. Stehlik, C. Eichler, X. Mi, T. R. Hartke, M. J. Gullans, J. M. Taylor, and J. R. Petta, Threshold dynamics of a semiconductor single atom maser, *Physical Review Letters* **119**, 097702 (2017).
- [32] M. Nomura, N. Kumagai, S. Iwamoto, Y. Ota, and Y. Arakawa, Laser oscillation in a strongly coupled single-quantum-dot–nanocavity system, *Nature Physics* **6**, 279–283 (2010).
- [33] O. Astafiev, K. Inomata, A. Niskanen, T. Yamamoto, Y. A. Pashkin, Y. Nakamura, and J. S. Tsai, Single artificial-atom lasing, *Nature* **449**, 588 (2007).
- [34] P. Neillinger, S. N. Shevchenko, J. Bogár, M. Reháč, G. Oelsner, D. S. Karpov, U. Hübner, O. Astafiev, M. Grajcar, and E. Il’ichev, Landau-zener-stückelberg-majorana lasing in circuit quantum electrodynamics, *Physical Review B* **94**, 094519 (2016).
- [35] P. Neillinger, M. Reháč, M. Grajcar, G. Oelsner, U. Hübner, and E. Il’ichev, Two-photon lasing by a superconducting qubit, *Physical Review B* **91**, 104516 (2015).
- [36] G. Oelsner, P. Macha, O. V. Astafiev, E. Il’ichev, M. Grajcar, U. Hübner, B. I. Ivanov, P. Neillinger, and H.-G. Meyer, Dressed-state amplification by a single superconducting qubit, *Physical review letters* **110**, 053602 (2013).
- [37] M. Kjaergaard, M. E. Schwartz, J. Braumüller, P. Krantz, J. I.-J. Wang, S. Gustavsson, and W. D. Oliver, Superconducting qubits: Current state of play, *Annual Review of Condensed Matter Physics* **11**, 369 (2020).
- [38] J. Koch, T. M. Yu, J. Gambetta, A. A. Houck, D. I. Schuster, J. Majer, A. Blais, M. H. Devoret, S. M. Girvin, and R. J. Schoelkopf, Charge-insensitive qubit design derived from the cooper pair box, *Physical Review A* **76**, 042319 (2007).
- [39] R. Ma, B. Saxberg, C. Owens, N. Leung, Y. Lu, J. Simon, and D. I. Schuster, A dissipatively stabilized mott insulator of photons, *Nature* **566**, 51 (2019).
- [40] K. W. Murch, U. Vool, D. Zhou, S. J. Weber, S. M. Girvin, and I. Siddiqi, Cavity-assisted quantum bath engineering, *Physical review letters* **109**, 183602 (2012).
- [41] A. Shabani and H. Neven, Artificial quantum thermal bath: Engineering temperature for a many-body quantum system, *Physical review A* **94**, 052301 (2016).
- [42] M. E. Kimchi-Schwartz, L. Martin, E. Flurin, C. Aron, M. Kulkarni, H. E. Tureci, and I. Siddiqi, Stabilizing entanglement via symmetry-selective bath engineering in superconducting qubits, *Physical review letters* **116**, 240503 (2016).
- [43] A. Soare, H. Ball, D. Hayes, X. Zhen, M. C. Jarratt, J. Sastrowan, H. Uys, and M. J. Biercuk, Experimental bath engineering for quantitative studies of quantum control, *Physical review A* **89**, 042329 (2014).
- [44] P. Horak, K. M. Gheri, and H. Ritsch, Quantum dynamics of a single-atom cascade laser, *Physical Review A* **51**, 3257 (1995).
- [45] J. M. Fink, A. Dombi, A. Vukics, A. Wallraff, and P. Domokos, Observation of the photon-blockade breakdown phase transition, *Physical Review X* **7**, 011012 (2017).
- [46] S. André, P.-Q. Jin, V. Brosco, J. H. Cole, A. Romito, A. Shnirman, and G. Schön, Single-qubit lasing in the strong-coupling regime, *Physical review A* **82**, 053802 (2010).
- [47] B. W. Shore and P. L. Knight, The jaynes-cummings model, *Journal of Modern Optics* **40**, 1195 (1993).
- [48] C. Gardiner and M. Collett, Master equation and quantum langevin theory of input, output, and internal modes of linear and nonlinear quantum amplifiers, in *International Quantum Electronics Conference* (Optical Society of America, 1984) p. ThGG5.
- [49] J. R. Johansson, P. Nation, and F. Nori, Qutip: An open-source python framework for the dynamics of open quantum systems, *Computer Physics Communications* **183**, 1760 (2012).
- [50] A. Blais, R.-S. Huang, A. Wallraff, S. M. Girvin, and R. J. Schoelkopf, Cavity quantum electrodynamics for superconducting electrical circuits: An architecture for quantum computation, *Physical Review A* **69**, 062320 (2004).
- [51] M. Löffler and H. Walther, Atomic coherence effects in the ion-trap laser, *Optics communications* **150**, 131 (1998).
- [52] A. Dombi, A. Vukics, and P. Domokos, Bistability effect in the extreme strong coupling regime of the jaynes-cummings model,

The European Physical Journal D **69** (2015).

[53] A. F. Linskens, I. Holleman, N. Dam, and J. Reuss, Two-photon rabi oscillations, *Physical Review A* **54**, 4854 (1996).